Applied Catalysis B: Environmental 132–133 (2013) 408–415

Contents lists available at SciVerse ScienceDirect

Applied Catalysis B: Environmental

journal homepage: www.elsevier.com/locate/apcatb

Heterogeneous photo-enhanced conversion of carbon dioxide to formic acid with copper- and gallium-doped titania nanocomposites

P.L. Richardson [a], Marisa L.N. Perdigoto [b], W. Wang [a], Rodrigo J.G. Lopes [b,*]

[a] MSC Catalysis Research Laboratories, California Institute of Technology, Pasadena, CA 91135, USA
[b] CIEPQPF – Centro de Investigação em Engenharia dos Processos Químicos e Produtos da Floresta, GERSE – Group on Environmental, Reaction and Separation Engineering, Department of Chemical Engineering, University of Coimbra, Rua Sílvio Lima, Polo II – Pinhal de Marrocos, 3030-790 Coimbra, Portugal

ARTICLE INFO

Article history:
Received 6 October 2012
Received in revised form
26 November 2012
Accepted 30 November 2012
Available online 10 December 2012

Keywords:
Photo-reduction
Carbon dioxide
Copper
Gallium
Titania
Formic acid

ABSTRACT

Copper- and gallium-doped titania photocatalysts prepared by means of sol–gel technique were comparatively evaluated with commercial TiO_2 (P25) for the photo-reduction of carbon dioxide to formic acid. The laboratory-made Cu_x–Ga_{1-x}/TiO_2 nanocomposites have been thoroughly characterized in crystallographic, structural, morphological, and elemental composition analyses. XRD revealed photocatalysts owning the specific crystalline phases of anatase, β-Ga_2O_3 and Cu_2O, which allowed inferring on the doping phenomena of both transition and post-transition metals. The quasi-homogeneous deposition of a Ga and Cu layer has been identified from the TEM morphological characterization and the Brunauer–Emmett–Teller and Barrett–Joyner–Halenda techniques unveiled quantitative differences in textural properties among the mesoporous Ga- and Cu-doped titania photocatalysts by underlining a decrease of surface area when augmenting the gallium dose. The laboratory-made photocatalysts presented bandgaps higher than 3 eV and the DRS spectra underlined the optical absorption edge of the nanocomposites with a considerable shift to the visible light region. The elemental composition quantified by means of XPS reproduced the binding energies relative of Ti, Cu and Ga ($2p_{3/2}$, $2p_{1/2}$), and the K-edge XANES characterization confirmed the effective doping and modulation of the electronic properties of the laboratory-made photocatalysts. Several experimental runs have been carried out with $Cu_{0.78}$–$Ga_{0.22}/TiO_2$ exhibiting the highest formic acid yields (394 μmol/g_{cat}) as well as superior quantum efficiency (49%) and selectivity (0.84). Accordingly, the photo-reduction of CO_2 was considerably promoted by doping Ga and Cu into the titania substrate, which ultimately avoided the surface recombination of electron–hole pairs, thereby enhancing the photo-activity of Cu_x–Ga_{1-x}/TiO_2 nanocomposites.

1. Introduction

Carbon dioxide, methane, nitrous oxide, and chlorofluorocarbons are the most prominent greenhouse gases contributing to the global warming caused by the rising atmospheric emissions. These pose severe environmental issues during the last decades due to the high atmospheric concentrations of carbon dioxide especially owing to human activities [1]. A cost-effective and sustainable-attractive technology to deal with the intensification of fossil-based energy economy is to photocatalytically reduce the CO_2 by irradiating it with UV light at room temperature and pressure conditions [2–4].

Numerous semiconductor materials including TiO_2, ZnO, CeO_2, ZrO_2, NbO_5, and V_2O_5 have been investigated as photosensitive nanocomposites for the chemical reduction of carbon dioxide [5–7]. These photocatalysts are irradiated by UV light which energy surpasses the bandgap energy so the e_{cb}^- switched from the semiconductor valence band to the conduction band, leaving h_{vb}^+ in the valence band. The mechanistic pathway proceeds with the promoted e_{cb}^- and h_{vb}^+ in both photocatalytic oxidation of organic compounds [8–11], and photocatalytic reductions of carbon dioxide to carbon monoxide and hydrocarbons including methane, ethane, formaldehyde, methanol, and formic acid [12–15].

Typically, the photo-reduction of carbon dioxide has been investigated in aqueous solutions under alkaline conditions and applying near UV irradiation [2,3,5,6,16–18]. Notwithstanding the low solubility of CO_2, gaseous carbon dioxide has been photocatalytically reduced querying the effect of the structure-morphology of nanocomposites [12,13,17,19], the influence of operating parameters such as the wavelength of UV irradiation [14], reduction temperature [14,15], and reactor flow configuration [20]. In fact, titania-based photocatalysts have moderate photo-activity and revealed a significant stability under severe photo-irradiation conditions [15,20,21]. Gaseous water was successfully used to produce

* Corresponding author. Tel.: +351 239798758; fax: +351 239798703.
E-mail address: rodrigo@eq.uc.pt (R.J.G. Lopes).

0926-3373/$ – see front matter © 2012 Elsevier B.V. All rights reserved.
http://dx.doi.org/10.1016/j.apcatb.2012.11.045

methane and carbon monoxide, and pure hydrogen was used as a reducing agent for the photo-conversion of carbon dioxide completely to carbon monoxide [14].

Metal oxides with larger bandgaps were identified to be noticeably resistant to photocorrosion. Hence, titania-based materials have been mostly used in heterogeneous photocatalysis for gas- and liquid-phase reactions mainly due to the distinctive physicochemical properties as well as using modified TiO_2 supported on molecular sieves [22–25]. In this regard, several transition metals were combined and/or supported on titanium dioxide to evaluate the performance of CO_2 photoreduction under UVA and UVC irradiation [26–30]. However, comprehensive investigations have not been reported to increase the photocatalytic activity of TiO_2-based photocatalysts coupled with copper metal.

To the best of our knowledge, Cu and Ga supported on titanium dioxides are scarcely studied for the photocatalytic reduction of CO_2, and considering the specific band gap of copper and gallium, the resulting photocatalyst is regarded to advance the photoreduction of carbon dioxide with water. Herein, we investigate thoroughly the effect of Cu and Ga via doping sol–gel wet chemical technique, upon photocatalytic production of formic acid from CO_2, and evaluate that both the transition metal and post-transition metal deposition plays a major role in dictating the photocatalytic efficiency of Cu_x–Ga_{1-x}/TiO_2 nanocomposite. The purpose of this work is twofold: to characterize thoroughly copper and gallium-doped titania photocatalysts, as well as to query comprehensively the influence of alkaline conditions, UV irradiation wavelength, and microstructure of nanocomposites on the photocatalytic conversion of carbon dioxide to formic acid and its selectivity.

2. Experimental

2.1. Materials and preparation of Cu_x–Ga_{1-x}/TiO_2

A mixed solution (50 ml) of 0.75 M $Cu(NO_3)_3$ and 0.25 M gallium nitrate hydrate (Aldrich, >99.9%; $Ga(NO_3)_3{\cdot}nH_2O$) was dropped at a rate of 0.01 ml s^{-1} into 250 ml of a 0.055 M Na_2CO_3 solution in a vessel at 298.15 K with stirring at a rate of 650 rpm. 1 M NaOH has been used to adjust the pH (7.8), and the resulting solution was regularly stirred for 1.5 h (650 rpm) and regulating constantly the pH with 1.0 M NaOH. Subsequently, the mixture was heated at 358.15 K and maintained under vigorous agitation for 24 h. A polytetrafluoroethene-based membrane (Omnipore PTFE, Hydrophilic, 0.2 μm, 47 mm, 80% porosity, Millipore) was used to filter the metal precipitates. The resulting metal composites were further washed with deionized water (<1.0 μS cm^{-1}) and dried at room temperature (298 K) for 48 h.

For the comparison studies, titania was obtained from Degussa (TiO_2 P-25) in a nonporous powder formed by a mixture of anatase and rutile (80:20) with a BET surface area of about 50 m^2 g^{-1} and average primary particle size of about 30 nm. For the laboratory-made catalysts, the precursor was titanium(IV) butoxide ($Ti(OC_4H_9)_4$, 98% in *n*-butanol) as supplied from Sigma–Aldrich. Nitrogen was purged in an atmosphere characterized by 20% relative humidity to perform the hydrolysis step. The hydrolyzing water was consistently released by the esterification of butanol and acetic acid in order to circumvent precipitation at the polycondensation stage and also the generation of unstable colloidal sols. This methodology allows one to control the stoichiometric ratio as to carry out the hydrolysis of titanium butoxide with water. 0.01 mol titanium butoxide was then mixed with 0.04 mol anhydrous butanol (>99.7%) and 0.04 mol glacial acetic acid (>99.7%) for a representative batch step and the solution was kept under constant agitation until the pH become constant (≈3.7). Subsequently, the sol has been dried at 135 °C and further calcinated at 520 °C to remove completely the presence of organic compounds.

The copper and gallium dispersion of the laboratory-made catalysts was measured using the method of Chang et al. [31]. The immersion of Cu–Ga nanoparticles in the resulting solution was carried out as to prepare the following laboratory-made photocatalysts: Ga/TiO_2, Cu/TiO_2, $Cu_{0.17}$–$Ga_{0.83}/TiO_2$, $Cu_{0.52}$–$Ga_{0.48}/TiO_2$, $Cu_{0.78}$–$Ga_{0.22}/TiO_2$. Copper- and gallium-doped titania (Cu/TiO_2, Ga/TiO_2) and TiO_2 (P25) were impregnated accordingly, and the nanocomposites were further submitted to a calcination stage (550 °C). Ga- and Cu-doped titania has been reduced with continuous 5% H_2/Ar stream mixture for 3 h at 350 °C. Fresh and used nanocomposites have been comprehensively characterized by transmission electron microscopy (TEM), X-ray diffraction (XRD), X-ray photoelectron spectroscopy (XPS), X-ray absorption near-edge structure (XANES), UV–vis diffused reflectance spectroscopy, and BET/BJH techniques.

2.2. Photoreactor and experimental procedure

The photocatalyst powder (<0.1 g) was dispersed in a CO_2 solution (100 ml) in a down-window type irradiation cell made of Pyrex glass. Carbon dioxide was catalytically reduced in a continuous flow reactor. Carbon dioxide was preliminary adsorbed with different aqueous solutions of sodium hydroxide and potassium bicarbonate to enhance CO_2 solubility. The reactor was fed with pure carbon dioxide (>99.99%) to eliminate the solubilized oxygen from the bulk medium and further saturated with 0.5 M NaOH and 0.10 M $KHCO_3$.

Three different UV lamps were used with the following spectral ranges in preliminary tests. Two Hg lamps for near UV (350–450 nm) with 200 W and mid UV (280–350 nm) with 350 W, and a halogen-based lamp for deep UV (240–260 nm) with 500 W HgXe have been evaluated for the photocatalytic conversion of carbon dioxide. Given the wavelength range of the exposure lamps, a cooling system was coupled with a water pump as to keep the reaction system at room temperature. Unless stated otherwise, the photoreduction experiments have been carried out by using the halogen-based lamp for deep UV (240–260 nm) with 500 W HgXe. The wavelength–current spectra of both lamps with an incident light power evaluated at the reactor were: 200 W to 45 mW/cm^2 (410 nm) and 30 mW/cm^2 (370 nm); 350 W to 90 mW/cm^2 (410 nm) and 45 mW/cm^2 (370 nm); 500 W to 20 mW/cm^2 (260 nm). The halogen-based lamp for deep UV (240–260 nm) with 500 W HgXe was typically used for 24 h reaction time and after that, the final reaction products was centrifuged for analyzing them as well as the photocatalysts.

Formic acid was the predominant product for all the photocatalytic reductions of carbon dioxide as confirmed by gas chromatography (TCD/FID) after performing blank experiments to verify the hydrocarbon formation from the CO_2 conversion. The following methodology enabled to ascertain that hydrocarbons were not produced at identical experimental conditions as verified by blank experiments carried out under UV irradiation in the absence of catalyst and an additional set performed with the photocatalyst and carbon dioxide in the dark. Quantum yield of the reaction was calculated by the following equation $\eta_{quantum}$ (%) = (2 × moles of formic acid yield)/(mole of photon absorbed by catalyst) × 100. The number represents the two electrons required to convert the C^{4+} of CO_2 to the C^{2+} of formic acid.

2.3. Analytical techniques

Products and reaction intermediates have been quantified by gas chromatography (Shimadzu) equipped with a thermal conductivity detector (GC-8A), using packed columns of molecular sieve 13X-S

and polyethylene glycol (PEG-6000) supported on Flusin P 60/80 100 ml (GL Sciences Inc.). The reaction products were systematically analyzed by gas chromatography (GC-2010 Plus) equipped with a flame ionization detector (ZB-1 column $T = 170\,^{\circ}C$, injection $T = 250\,^{\circ}C$, determination $T = 280\,^{\circ}C$, split ratio 1:300, 0.2 μl). GC-FID detector is semi-cylindrical electrode type, quartz jet, DL 3×10^{-12} g/s for diphenyl, $T = 450\,^{\circ}C$ in $1\,^{\circ}C$ increments. Due to low sensitivity of FID to formic acid, the GC was equipped with a porapak Q column. TOC was measured with a *Shimadzu 5050 TOC Analyser*, which operates based on the combustion/nondispersive infrared gas analysis method. The parameter uncertainty in TOC measurement, quoted as the deviation of three separate measurements, was never larger than 2% for the range of the TOC concentrations.

The microstructure of the photocatalysts was analyzed by means of a JEM 2010 (Jeol) TEM microscope operated at an acceleration voltage of 200 kV with LaB_6 filament, and characterized by 0.23 nm point resolution, convergent-beam and nanobeam diffraction. It was equipped with Oxford Instruments ATW type EDS detector with INCA Energy TEM platform and elemental mapping using the INCA Semi-STEM mode. Regular single-tilt and double-tilt holders (heating stage <1200 °C) are serviced with a Be double-tilt holder and the tilting limit is ±30°. In all TEM analyzes, the specimens were prepared by suspending solid samples and further ultrasonicated for 1 h.

The textural properties and nitrogen sorption isotherms were determined by the volumetric technique at 77 K using nitrogen by a Micrometrics ASAP 2010 sorptometer. The samples were preliminary submitted to over-drying at 80 °C and evacuated overnight under vacuum condition. The surface area was quantified using Brunauer–Emmett–Teller (BET) surface analysis based on adsorption data in the partial pressure (P/P_0) range 0.05–0.95. The amount of nitrogen adsorbed at $P/P_0 = 0.995$ was used to calculate the total pore volume and the average pore size was found from the adsorption data by Barrett–Joyner–Halenda (BJH) porosity method.

X-ray diffractograms were recorded for evaluating the catalyst crystallinity by means of powder X-ray diffraction in a Philips EXPERT θ–2θ X-ray diffractometer with Cu Kα radiation ($\alpha = 1.53$ Å) from 10° to 90° 2θ at a scanning speed of $0.03^{\circ}\ s^{-1}$. The X-ray tube voltage and current were set at 35 kV and 45 mA, respectively. The line broadening of anatase TiO_2 reflection plane ($2\theta = 48^{\circ}$) has been used to probe the crystallite size pointing out that there was negligible interference from the photocatalysts.

X-ray photoelectron spectroscopy data were carried out with a Thermo VG Scientific Sigma Probe spectrometer using Al Kα radiation at 15 kV, 25 mA, pass energy 22.0 eV. The base pressure in the analyzing chamber was preserved in the range of 2×10^{-8} to 6×10^{-9} Torr. The binding energy of XPS spectra was adjusted by the carbon reference value: 285.0 eV. Depth-profile measurements was additionally performed using Ar^+ etching for 20 min to investigate the core of the Ga- and Cu-loaded titania photocatalysts.

Optical spectroscopic measurements were performed with UV–vis spectrophotometer (JASCO V-650) using D_2 and halogen lamps for wavelengths below and above 335 nm, respectively. The diffuse reflectance measurements were accomplished by means of an integrating sphere (JASCO ISV-469) and the measurements have been recorded at 280 K for wavelengths in the range 200–800 nm with 0.1 g of fresh and used catalysts. The Kubelka–Munk function has been applied to convert the DRS data to absorption spectra, and the Davis–Mott model was used to estimate the bandgap (E_g) of the laboratory-made photocatalysts.

Ga, Cu, and Ti K-edge X-ray absorption fine structure (XAFS) spectra were measured at 40–290 K in transmission mode in the PT Synchrotron Laboratory on beamline 3C1Ax. The storage-ring energy and the ring current were 2.5 GeV and 300 mA, respectively. The X-ray beam path was prepared with a Si(1 1 1) double-crystal monochromator and the X-ray intensity was kept at 80% of the maximum flux by means of a piezo converter set to the crystal. The characteristic dimensions of the slit was 1–2 mm (height) × (1–4) mm (width) in front of the I_0 ionization chamber. Nitrogen and argon were used to purge the I_0 and I_t ionization chambers, respectively. Different scanning velocities were used to process the pre-edge, edge, and postedge regions as ≈6, ≈0.4, and ≈2 eV, respectively and implementing a data sampling time of 8 s (max) for the collecting point. The energy accuracy of the monochromator was replicated within ±0.1 eV. The following XAFS K-edge absorption energy values were used to calibrate the spectra of Ga, Cu, and Ti: 10368.3, 8980.1, and 4971.1 eV, respectively [32].

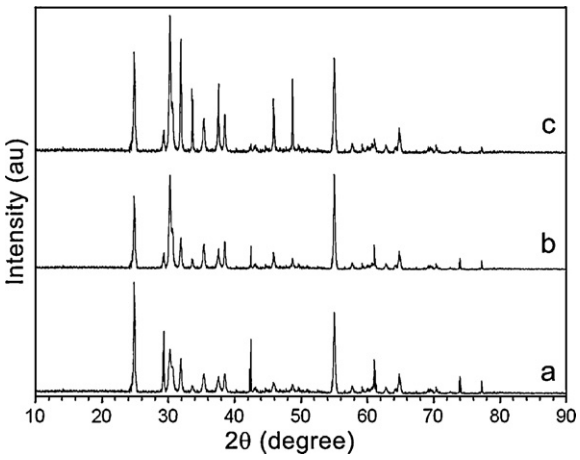

Fig. 1. X-ray diffractogram of laboratory-made (a) $Cu_{0.78}$–$Ga_{0.22}/TiO_2$, (b) $Cu_{0.52}$–$Ga_{0.48}/TiO_2$, and (c) $Cu_{0.17}$–$Ga_{0.83}/TiO_2$ photocatalysts.

3. Results

3.1. XRD structure of photocatalysts

The phase structure and composition of Ga- and Cu-doped titania photocatalysts have been characterized by powder X-ray diffraction analyzes. Fig. 1 shows the XRD patterns of the $Cu_{0.17}$–$Ga_{0.83}/TiO_2$, $Cu_{0.52}$–$Ga_{0.48}/TiO_2$, $Cu_{0.78}$–$Ga_{0.22}/TiO_2$ nanocomposites. As can be seen, the characteristic peaks at $2\theta = 30.3^{\circ}$, 31.8°, 33.5°, 35.4°, 37.6°, 38.5°, 43.5°, 46.2°, 48.8°, 49.9°, and 54.8° correspond to the (0 0 4), (2 0 0), (1 1 −1), (1 1 1), (1 0 4), (1 1 −3), (1 1 3), (0 0 6), (0 1 5), (2 0 4), and (1 1 5) planes of crystalline β-Ga_2O_3, respectively. These diffraction peaks (JCPDS Card No. 11-370) identifies not only the gallium oxide phase (β-Ga_2O_3) as anticipated from the particular annealing temperatures, but additionally pointed out no additional impurity diffraction from the parent semiconductor oxide. The diffraction peaks at $2\theta = 36.5^{\circ}$, 42.6°, 52.7°, and 61.8° can be assigned to the (1 1 1), (0 2 0), (1 2 1), and (2 0 2) planes of crystalline cuprous oxide (JCPDS Card No. 78-2076), respectively. X-ray diffraction patterns of both Cu_x–Ga_{1-x}/TiO_2 nanocomposites demonstrated similarities between the X-ray diffraction pattern of titania and that of gallium and copper doped TiO_2. This fact indicated that both transition metals were doped onto the surface matrix of the titanium dioxide (Ga and Cu).

The XRD diffractograms of $Cu_{0.17}$–$Ga_{0.83}/TiO_2$, $Cu_{0.52}$–$Ga_{0.48}/TiO_2$, $Cu_{0.78}$–$Ga_{0.22}/TiO_2$ also revealed the characteristic crystallographic structure of titania. The calcination temperature between 450 and 550 °C enabled producing different crystalline nanocomposites with XRD patterns specific of anatase phase according to Fig. 1. The diffraction peaks at $2\theta = 25.3^{\circ}$, 33.1°, 38.4°, 47.5°, 51.5°, 69.4° are relative to (2 0 0), (2 1 1), (2 2 0), (2 2 2), (2 3 1), (4 2 2) planes of crystalline anatase (JCPDS Card No.

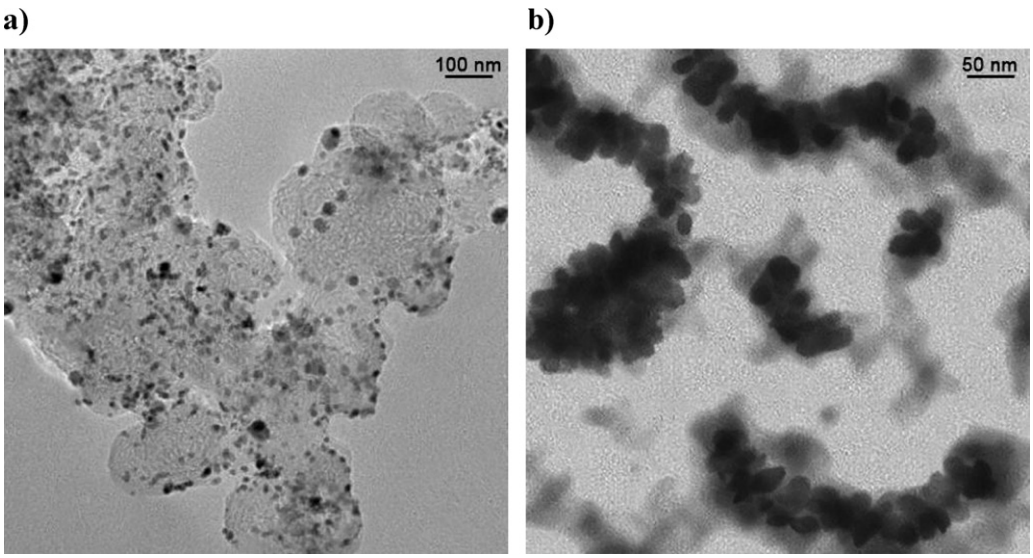

Fig. 2. Transmission electron microscopy patterns of the laboratory-made $Cu_{0.78}$–$Ga_{0.22}/TiO_2$ photocatalyst.

21-1272), respectively. Conversely, as the calcination temperature was higher than 600 °C the anatase phase is most likely transformed into rutile-like crystalline phases. The Cu_x–Ga_{1-x}/TiO_2 nanocomposites have developed an amorphous microstructure by conferring different ratios of anatase/rutile phases. Indeed, the following diffraction peaks were identified for higher calcination temperatures: 27.5°, 36.1°, 41.3°, 54.4°, 56.7°, 69.1° which corresponds to (1 1 0), (1 0 1), (1 1 1), (2 1 1), (2 2 0), (3 0 1) diffractions, respectively. Consequently, laboratory-made photocatalysts have been calcinated at 550 °C in order to prepare the Ga/TiO_2, Cu/TiO_2, $Cu_{0.17}$–$Ga_{0.83}/TiO_2$, $Cu_{0.52}$–$Ga_{0.48}/TiO_2$, $Cu_{0.78}$–$Ga_{0.22}/TiO_2$ nanocomposites for the photo-conversion of carbon dioxide into formic acid.

3.2. TEM patterns of photocatalysts

Cu_x–Ga_{1-x}/TiO_2 nanocomposites have been morphologically characterized by means of transmission electron microscopy. Representative TEM patterns of different magnifications are depicted in Fig. 2 for the $Cu_{0.78}$–$Ga_{0.22}/TiO_2$ photocatalyst. As can be seen, the Ga- and Cu-loaded nanocomposites have characteristic grain sizes lower than 40 nm, which pointed out the particle size obtained via the sol–gel preparation technique. The $Cu_{0.78}$–$Ga_{0.22}/TiO_2$ nanocomposite exhibited a homogeneous size distribution and regular shape within the range 25–35 nm in terms of diameter. Hence, the dispersion of both transition metals attained on the titanium dioxide framework allowed obtaining a well-defined nanocomposite size, which dictate its reactivity during the chemical reduction of carbon dioxide to formic acid. In this regard, the sol–gel synthesis avoided somewhat the formation of fibrous nanomaterials for titania-based photocatalysts. According to Fig. 2, the copper- and gallium-doping layer also indicated the uniform deposition of both transition metals that have been additionally inspected for fresh and used specimens as to evaluate how the catalytic stability was affected in terms of nanomaterial morphology.

The influence of calcination temperature has been also investigated by carrying out TEM analyzes under different curing stages. This fact led to the identification of optima conditions for the photocatalytic reduction of carbon dioxide so TEM patterns were performed preliminary to the curing stage and after that as to identify the desired grain size of Cu_x–Ga_{1-x}/TiO_2 nanocomposites. The commercial titania exhibited a bimodal particle size distribution with the following prevailing dimensions 48 and 71 nm, whereas the particle size distribution of gallium- and copper-loaded titania nanocomposites has been assessed and the mean particle sizes were considerably within the range 25–35 nm, thereby highlighting the sol–gel synthesis as an effective technique to produce gallium- and copper-doped titania nanocomposites.

3.3. BET and BJH analyzes

Gallium- and Cu-doped titania nanocomposites have been characterized through BET and BJH analyses by means of an accelerated surface area and porosimetry analyzer. Fig. 3a shows the BET isotherm of fresh and used (10 h) $Cu_{0.78}$–$Ga_{0.22}/TiO_2$. The Brunauer–Emmet–Teller isotherm mimics the textural properties of type IV isotherms. The remainder of the titania-based photocatalysts prepared via the sol–gel route also pointed out a mesoporous structure for Ga- and Cu-loaded nanocomposites ($Cu_{0.17}$–$Ga_{0.83}/TiO_2$, $Cu_{0.52}$–$Ga_{0.48}/TiO_2$, and $Cu_{0.78}$–$Ga_{0.22}/TiO_2$).

Table 1 shows the surface area and pore volume of TiO_2 (P25), Ga/TiO_2, Cu/TiO_2, $Cu_{0.17}$–$Ga_{0.83}/TiO_2$, $Cu_{0.52}$–$Ga_{0.48}/TiO_2$, $Cu_{0.78}$–$Ga_{0.22}/TiO_2$ prepared with different molar proportions as well as the crystal sizes and bandgap energies of the gallium- and copper-doped photocatalysts. The total pore volume was determined by the adsorption at a relative pressure of 0.995 for N_2 at 77 K, and the $d_{crystal}$ is the calculated crystal size from XRD spectra of calcined samples. The highest surface area was for the commercial catalyst (TiO_2 P25, 50 $m^2\,g^{-1}$), while the lower was obtained for the laboratory-made $Cu_{0.78}$–$Ga_{0.22}/TiO_2$ with 24 $m^2\,g^{-1}$. The higher bandgaps were obtained for TiO_2 (P25) and Ga/TiO_2 with 3.47 and 3.27 eV, respectively; while the laboratory-made catalysts including $Cu_{0.17}$–$Ga_{0.83}/TiO_2$, $Cu_{0.52}$–$Ga_{0.48}/TiO_2$, $Cu_{0.78}$–$Ga_{0.22}/TiO_2$ exhibited bandgaps higher than 3 eV with the

Table 1
Brunauer–Emmet–Teller surface area (S_{BET}), pore volume (V_{pore}), crystal sizes and bandgap energies of TiO_2 (P25) and gallium- as well as copper-doped titania photocatalysts prepared with different molar proportions.

	S_{BET} ($m^2\,g^{-1}$)	V_{pore} ($cm^3\,g^{-1}$)	$d_{crystal}$ (nm)	E_g (eV)
TiO_2 (P25)	50	–	23	3.47
Ga/TiO_2	46	0.068	31	3.27
Cu/TiO_2	32	0.030	20	2.89
$Cu_{0.78}$–$Ga_{0.22}/TiO_2$	24	0.051	15	3.14
$Cu_{0.52}$–$Ga_{0.48}/TiO_2$	37	0.041	19	3.01
$Cu_{0.17}$–$Ga_{0.83}/TiO_2$	41	0.037	18	3.03

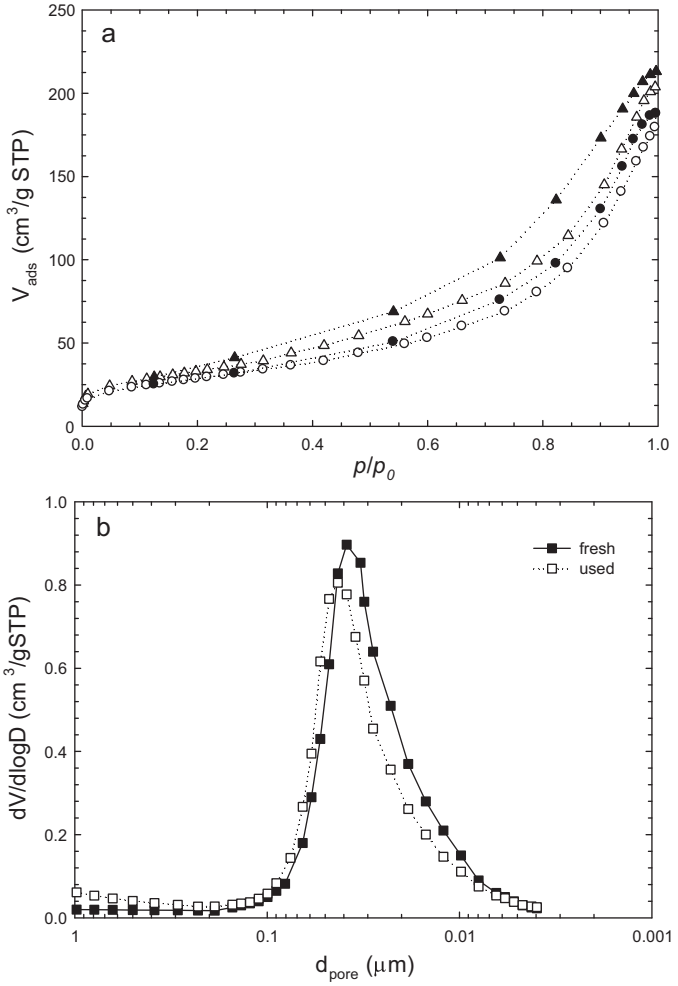

Fig. 3. (a) Brunauer–Emmet–Teller isotherm and (b) porosity size distribution of $Cu_{0.78}$–$Ga_{0.22}/TiO_2$ photocatalyst (△, Ads:cat_{fresh}; ▲, Des:cat_{fresh}; ○, Ads:cat_{used}; ●, Des:cat_{used}).

exception of Cu/TiO_2. In fact, the crystalline structure of titanium dioxides assumes a major role in controlling the bandgap, which can be also ascribed with the morphology and structure of titania-based photocatalysts when prepared via the sol–gel route.

Fig. 3b plots the pore size distribution of fresh and used $Cu_{0.78}$–$Ga_{0.22}/TiO_2$ samples. As can be seen, a narrow profile has been identified for the copper- and gallium-doped photocatalysts. In fact, doping the titania framework with more copper led to the decrease of surface area, which can be ascribed to the morphological structure of the coating layer. The tabulated data also indicated that the gallium- and copper-doped titania nanocomposites had similar Barrett–Joyner–Halenda properties regarding the pore volume of Cu_x–Ga_{1-x}/TiO_2 photocatalysts compared to commercial titania. The relative structural density of titanium dioxide shell gave rise to the high crystal size, which is ultimately dictated by the stoichiometric ratio of Ti/O during the nanocomposite formulation. This fact is in agreement with the transmission electron microscopy patterns and underlined how the nanocomposite morphology was affected in terms of crystal size. According to Table 1, $Cu_{0.78}$–$Ga_{0.22}/TiO_2$ exhibited the smallest crystal size in comparison to the highest crystal size revealed by Ga/TiO_2. Therefore, the structural characterization accomplished both for the BJH and BET properties pointed out remarkable differences for the gallium- and copper-doped titania nanocomposites.

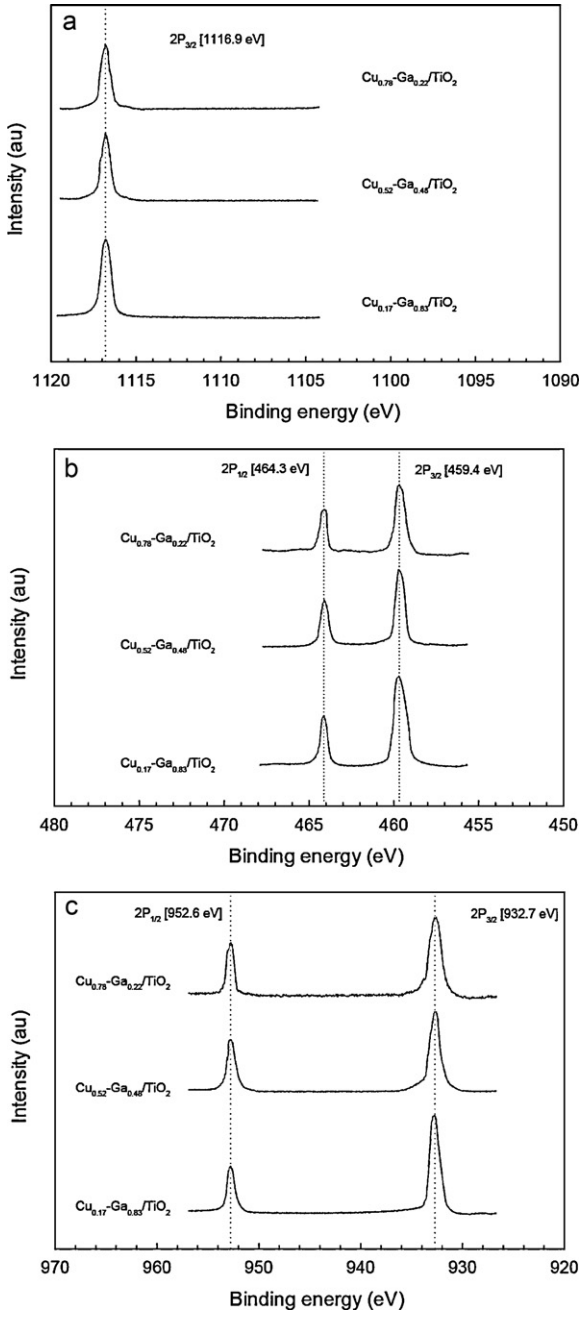

Fig. 4. X-ray photoelectron spectra of (a) Ga $2p_{3/2}$, (b) Ti ($2p_{3/2}$, $2p_{1/2}$), (c) Cu ($2p_{3/2}$, $2p_{1/2}$) in $Cu_{0.78}$–$Ga_{0.22}/TiO_2$, $Cu_{0.52}$–$Ga_{0.48}/TiO_2$, and $Cu_{0.17}$–$Ga_{0.83}/TiO_2$ photocatalysts.

3.4. XPS characterization

Fig. 4 shows the X-ray photoelectron spectra of the Cu_x–Ga_{1-x}/TiO_2 nanocomposites. As can be seen, the XPS spectra pointed out that the gallium metal has been doped into the titanium dioxide structure. The XPS spectra of Ti ($2p_{3/2}$, $2p_{1/2}$) for copper- and gallium-doped photocatalysts exhibited characteristic binding energies that are close to those of titanium dioxide at 459.4 and 464.3 eV (Fig. 4b). The chemical structure of titania was modified during the preparation technique with gallium and copper transition metal dopants. Fig. 4c shows the XPS spectra of Cu ($2p_{3/2}$, $2p_{1/2}$) and the characteristic binding energies at 932.7 and 952.6 eV, demonstrating its doping into the surface of titanium dioxide photocatalysts. The binding energy of Ga $2p_{3/2}$ has also

Table 2
Element molar ratio of gallium- and copper-loaded photocatalysts calculated from X-ray photoelectron spectroscopy and from hydrothermally etching preparation technique (*bulk*).

	Ga/Ti		Cu/Ti		Ga/Cu	
	XPS	*bulk*	XPS	*bulk*	XPS	*bulk*
Ga/TiO_2	0.123	0.037	–	–	–	–
Cu/TiO_2	–	–	0.175	0.042	–	–
$Cu_{0.78}–Ga_{0.22}/TiO_2$	0.029	0.011	0.161	0.029	0.180	0.379
$Cu_{0.52}–Ga_{0.48}/TiO_2$	0.078	0.021	0.088	0.013	0.886	1.615
$Cu_{0.17}–Ga_{0.83}/TiO_2$	0.107	0.028	0.043	0.009	2.488	3.111

been identified at 1116.9 eV for the gallium- and copper-doped titania nanocomposites ($Cu_{0.17}–Ga_{0.83}/TiO_2$, $Cu_{0.52}–Ga_{0.48}/TiO_2$ and $Cu_{0.78}–Ga_{0.22}/TiO_2$), as illustrated in Fig. 4a.

Table 2 shows the elemental chemical composition of gallium- and copper-doped nanocomposites probed by means of X-ray photoelectron spectroscopy for Ga and Cu transition metals. The *bulk* normalized composition was also directly estimated from the sol–gel preparation technique. While the *bulk* composition reflects the quantification at the innermost and the outermost surface of the nanocomposite dealing with the titania core structure, the XPS-derived value only indicates the elemental chemical composition at the outermost surface of the $Cu_x–Ga_{1-x}/TiO_2$ photocatalysts. From the comparison between the composition of $Cu_{0.17}–Ga_{0.83}/TiO_2$, $Cu_{0.52}–Ga_{0.48}/TiO_2$, and $Cu_{0.78}–Ga_{0.22}/TiO_2$ nanocomposites, considerable differences were found as can be seen from the tabulated data. This fact pointed out the $Cu_{0.78}–Ga_{0.22}/TiO_2$ specimen with the highest copper/gallium ratio, whereas the $Cu_{0.17}–Ga_{0.83}/TiO_2$ nanocomposite showed the highest Ga/Cu composition ratio among the copper- and gallium-doped photocatalyst synthesized via the sol–gel route.

3.5. Diffuse reflectance spectroscopy

Gallium- and copper-doped titania nanocomposites have been characterized by means of UV–vis diffuse reflectance spectroscopy for the $Cu_x–Ga_{1-x}/TiO_2$ photocatalysts. The DRS spectra of Ga/TiO_2, Cu/TiO_2, $Cu_{0.17}–Ga_{0.83}/TiO_2$, $Cu_{0.52}–Ga_{0.48}/TiO_2$, $Cu_{0.78}–Ga_{0.22}/TiO_2$ are shown in Fig. 5. The TiO_2 (P25) revealed practically no absorption of visible light mainly due to the large bandgap energy computed and shown in Table 1: 3.5 eV. However, after doping the titania photocatalyst with gallium and copper metals, the optical absorption edge of the nanocomposites presented an considerable shift to the visible light region. Moreover, the bandgap values

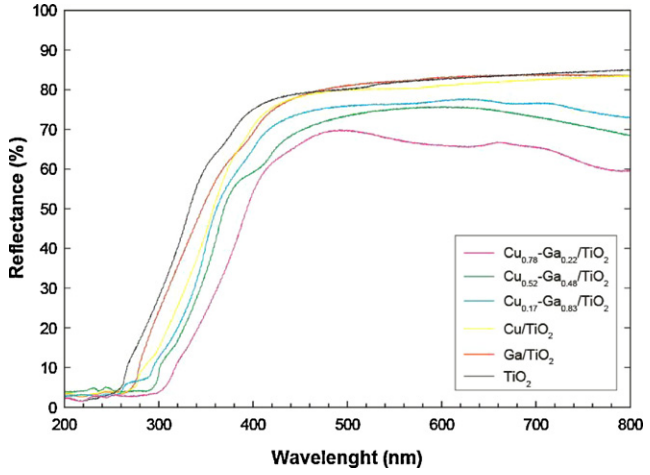

Fig. 5. Diffuse reflectance UV–vis spectra of $Cu_{0.78}–Ga_{0.22}/TiO_2$, $Cu_{0.52}–Ga_{0.48}/TiO_2$, and $Cu_{0.17}–Ga_{0.83}/TiO_2$ photocatalysts.

calculated with the Davis and Mott model in the range 2.9–3.5 eV are indicative of the photo-activity for the $Cu_x–Ga_{1-x}/TiO_2$ nanocomposites. By applying the Kubelka–Munk function versus the bandgap energy, the remainder of the specimens was characterized so the Cu/TiO_2 exhibited the smallest bandgap energy. Hence, the DRS spectra indicated that both the transition and post-transition metals allowed attaining a remarkable visible light absorption in the range 360–390 nm.

3.6. XANES

Gallium- and copper-doped titania nanocomposites have been characterized by X-ray absorption near-edge structure analyses. Fig. 6a depicts the Ga K-edge XANES spectra and a specific shift was found for all photocatalysts so the most intense peak appeared as follows: 10368.3, 10368.7, and 10369.1 eV for $Cu_{0.78}–Ga_{0.22}/TiO_2$, $Cu_{0.52}–Ga_{0.48}/TiO_2$, and $Cu_{0.17}–Ga_{0.83}/TiO_2$ respectively. In fact, the following energy gaps were identified for the $Cu_{0.78}–Ga_{0.22}/TiO_2$: 3.8, 5.7, 8.6 eV, $Cu_{0.52}–Ga_{0.48}/TiO_2$: 4.5, 4.1, 9.0 eV, and $Cu_{0.17}–Ga_{0.83}/TiO_2$: 5.3, 4.4, 8.6 eV. These Ga K-edge XANES spectra indicated that the post-transition metal was effectively doped into the titania substrate. Ti K-edge XANES spectra are shown comparatively in Fig. 6b for the laboratory-made $Cu_x–Ga_{1-x}/TiO_2$ photocatalysts. Both gallium- and copper-doped nanocomposites revealed analogous XANES patterns as can be seen for the spectral range 4950–5000 eV. Indeed, the highest intense peaks were found at 4970.5, 4971.2, and 4971.6 eV for $Cu_{0.78}–Ga_{0.22}/TiO_2$, $Cu_{0.52}–Ga_{0.48}/TiO_2$, and $Cu_{0.17}–Ga_{0.83}/TiO_2$, respectively. At the edge and postedge regions, less intense and broad peaks positioned at (4974.6 and 4979.6) for $Cu_{0.78}–Ga_{0.22}/TiO_2$, and these gave the following energy gaps: (4.1 and 5) eV as well as (3.7, 7.4, and 12.9), (5.9, 7.4, and 12.0) eV for $Cu_{0.52}–Ga_{0.48}/TiO_2$, $Cu_{0.17}–Ga_{0.83}/TiO_2$, respectively. Fig. 6c depicts the Cu K-edge XANES spectra for the gallium- and copper-doped nanocomposites. $Cu_{0.78}–Ga_{0.22}/TiO_2$, $Cu_{0.52}–Ga_{0.48}/TiO_2$, and $Cu_{0.17}–Ga_{0.83}/TiO_2$ exhibited the following energy gaps: (3.2, 6.8, and 12.4), (3.6, 6.9, and 14.7), (3.2, 6.9, and 11.7) eV, respectively. Hence, the relative intensity of the first postedge peak in the Cu K-edge XANES spectra is accompanied by the energy shift found in the Ti K-edge spectra, thereby demonstrating specific interaction of copper sites with the titania-based structure. This behavior can be also identified when doping the nanocomposite with gallium so the resulting photocatalyst was effectively modulated in terms of electronic properties for the photo-conversion of CO_2 to formic acid.

3.7. Photo-activity and selectivity

Several photocatalytic reduction experiments have been carried out to evaluate the photo-activity in terms of formic acid yield. Fig. 7 presents the formic acid production at UV-300 nm as a function of reaction time for the commercial and laboratory-made photocatalysts (0.5 g/l) prepared via the sol–gel technique. The formic acid yields were 235.8, 190.3, 155.8, 64.3, 108.9, and 29.0 $\mu mol/g_{cat}$ after 5 h for $Cu_{0.78}–Ga_{0.22}/TiO_2$, $Cu_{0.52}–Ga_{0.48}/TiO_2$, $Cu_{0.17}–Ga_{0.83}/TiO_2$, Cu/TiO_2, Ga/TiO_2, and TiO_2 (P25), respectively. Under different UV irradiation wavelengths, Fig. 8 shows the formic acid yield for the copper- and gallium-doped titania nanocomposites. As can be seen, the highest photoconversions were obtained with the $Cu_{0.78}–Ga_{0.22}/TiO_2$ specimen, whereas the lowest formic acid yields were achieved with the commercial titanium dioxide (P25). In fact, 394.0, 383.8, 253.1 $\mu mol/g_{cat}$ was obtained for the $Cu_{0.78}–Ga_{0.22}/TiO_2$, while the TiO_2 (P25) gave 170.4, 112.9, 81.2 $\mu mol/g_{cat}$ after 10 h. Table 3 presents the formic acid and total organic carbon yield after 10 h irradiation time as well as the selectivity to formic acid and quantum efficiency ($\eta_{quantum}$) for

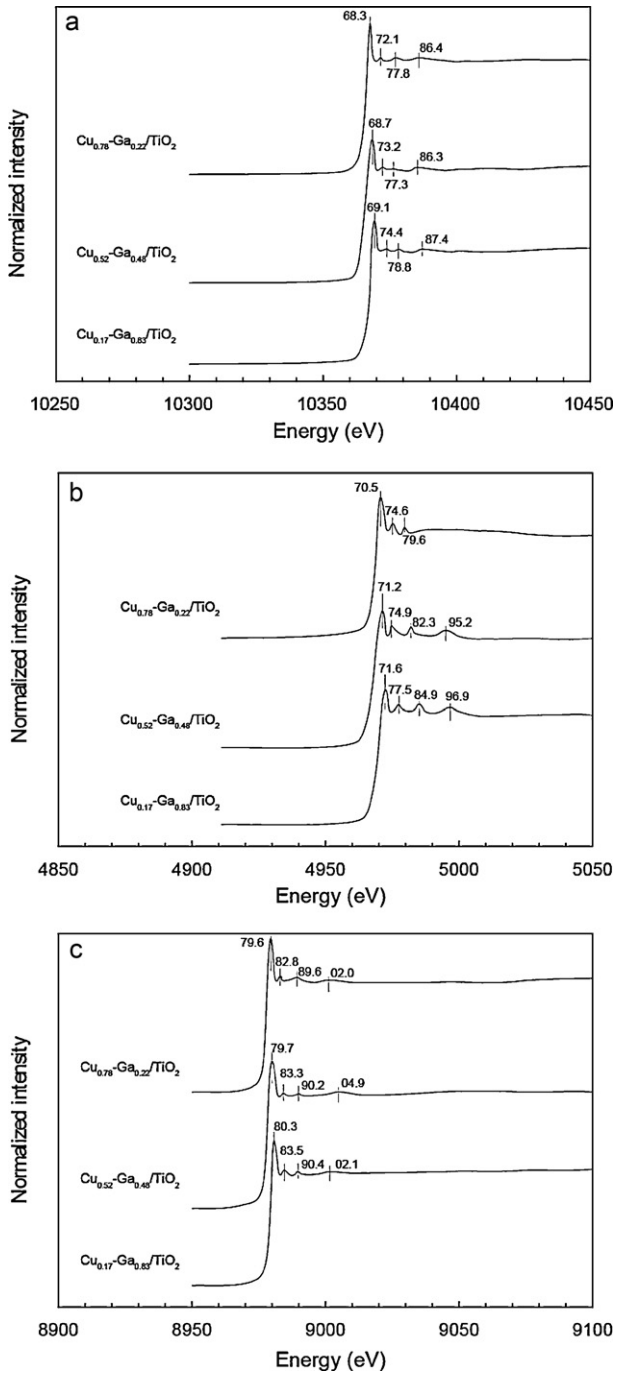

Fig. 6. X-ray absorption near-edge structure spectra of (a) Ga K-edge, (b) Ti K-edge, and (c) Cu K-edge for $Cu_{0.78}$–$Ga_{0.22}/TiO_2$, $Cu_{0.52}$–$Ga_{0.48}/TiO_2$, and $Cu_{0.17}$–$Ga_{0.83}/TiO_2$ photocatalysts.

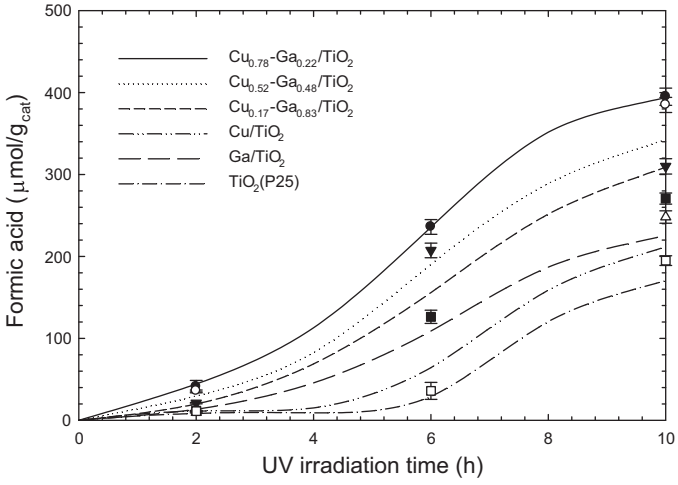

Fig. 7. Formic acid yield at UV-300 nm for $Cu_{0.78}$–$Ga_{0.22}/TiO_2$, $Cu_{0.52}$–$Ga_{0.48}/TiO_2$, $Cu_{0.17}$–$Ga_{0.83}/TiO_2$, Cu/TiO_2, Ga/TiO_2, and TiO_2 (P25) photocatalysts (0.5 g/l).

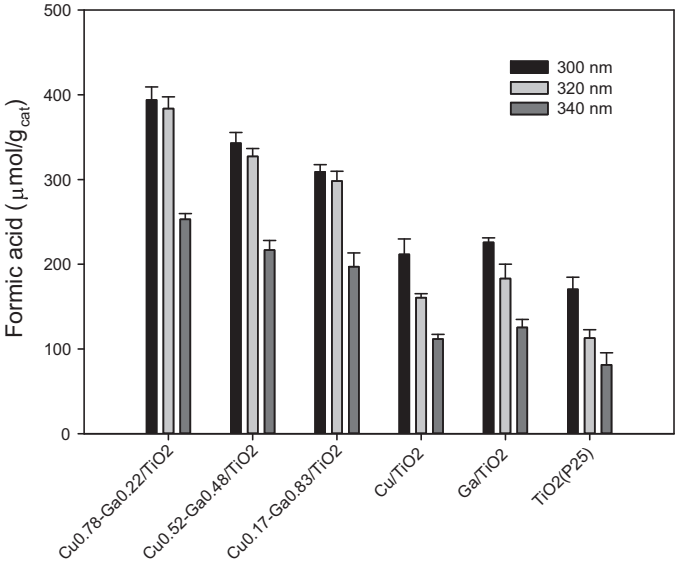

Fig. 8. Formic acid yield for the copper- and gallium-doped titania nanocomposites under different UV–vis irradiation wavelengths after 10 h (0.5 g/l).

gallium- and copper-doped titania nanocomposites at UV-300 nm. The maximum total organic carbon achieved with the laboratory-made nanocomposite $Cu_{0.78}$–$Ga_{0.22}/TiO_2$ was 467.6 μmol/g_{cat} and 19.48 μmol/m^2_{cat}, while the commercial titania (P25) presented the lowest quantum efficiency. The highest selectivity (0.84) was obtained with the $Cu_{0.78}$–$Ga_{0.22}/TiO_2$ photocatalyst, which exhibited also the highest quantum efficiency (48.9).

The formic acid formation and minor carbon monoxide formation using the $Cu_{0.78}$–$Ga_{0.22}/TiO_2$ specimen was validated for as long as 50 h, pointing out the suitability of the nanocomposite to adsorb carbon dioxide and photo-chemically reducing it to low molecular weight carboxylic acid under continuous UV and/or

Table 3
Formic acid and total organic carbon yield after 10 h irradiation time, selectivity to formic acid and quantum efficiency ($\eta_{quantum}$) for gallium- and copper-doped titania nanocomposites at UV-300 nm.

	Formic acid (μmol/g_{cat})	Formic acid (μmol/m^2_{cat})	TOC (μmol/g_{cat})	TOC (μmol/m^2_{cat})	Selectivity	$\eta_{quantum}$ (%)
TiO_2 (P25)	170.4	3.41	312.4	6.25	0.55	6.9
Ga/TiO_2	225.9	4.91	364.1	7.92	0.62	13.0
Cu/TiO_2	211.7	6.61	274.3	8.57	0.77	28.2
$Cu_{0.78}$–$Ga_{0.22}/TiO_2$	394.0	16.42	467.6	19.48	0.84	48.9
$Cu_{0.52}$–$Ga_{0.48}/TiO_2$	343.0	9.27	412.7	11.15	0.83	39.6
$Cu_{0.17}$–$Ga_{0.83}/TiO_2$	309.2	7.54	387.5	9.45	0.80	36.0

visible light. The slight decrease of the formic acid production rate has been attributed to its re-adsorption on the nanocomposite in comparison to the production rate for carbon monoxide, so further re-adsorption $Cu_{0.78}$–$Ga_{0.22}/TiO_2$ should occur at less extent. Therefore, the copper metal played the photocatalytic role by binding carbon dioxide and correlating it with protons and photogenerated electrons using a Cu^I/Cu^{II} redox couple. The pair binding between this transition metal and carbon dioxide affects concomitantly the multiple scattering regions of gallium sites, contributing to the production of carbonate-like species. Depending on the selectivity of the Cu_x–Ga_{1-x}/TiO_2 photocatalysts, these intermediate compounds are then transformed not only to formic acid but also formaldehyde and methanol, which have been quantified in terms of total organic carbon production normalized by catalyst amount and surface area (Table 3). Hence, the mechanism most likely followed the promotion via utilizing the Cu^I/Cu^{II} redox couple at the first steps, and further evolved to the complete reduction of carbon dioxide into formic acid. Given that formaldehyde and methanol was detected in small quantities, it may be readily transformed into the final products as characterized by means of GC in the gas-phase sampling of the heterogeneous catalytic system. XANES patterns of gallium- and copper-doped nanocomposites revealed similar energy gaps, which confirmed the doping phenomena, and exhibited also narrower profiles obtained for the most active photocatalyst. For the most HCOOH-selective, the intensity of the first postedge peak at the Ga K-edge decreased in comparison to that for the fresh one in vacuum at 298 K, while the Cu K postedge peak intensity increased in CO_2 at the same conditions. This characterization in the presence of carbon dioxide gave rise to the desorption–adsorption behavior monitored at the Cu K-edge, which was also identified in the Ga K-edge spectra. The ratio between the peak increase due to CO_2 sorption and the peak decrease caused by the physic-chemical desorption was calculated as the recovery extent. From the normalized XANES spectra, the recovery extent was Cu (34%) > Ga (7%) for the first postedge peak intensity.

Additionally, increasing the UV wavelength to 340 nm the CO_2 conversion decreased slightly notwithstanding the considerable formic acid yield attained with the laboratory-made Cu_x–Ga_{1-x}/TiO_2 nanocomposites. Hence, the photocatalytic reduction of carbon dioxide was improved when using gallium and copper-doped titania catalysts so the $Cu_{0.78}$–$Ga_{0.22}/TiO_2$ specimen gave the highest yields, and both the transition metal (Cu/TiO_2) or the post-transition metal (Ga/TiO_2) provided higher CO_2 conversions when compared with the commercial catalyst. The low photo-activity achieved for UV irradiation wavelengths higher than 420 nm is mainly due to the UV–vis absorption edge from the quantification of the diffuse reflectance spectra (Fig. 5). The formic acid yields achieved with the laboratory-made catalysts are intrinsically related with the sol–gel preparation technique as to obtain doped photocatalytic structures of titania with copper and gallium elements. This fact allowed optimizing the electronic properties of both nanocomposites to improve the distribution of Fermi levels and concomitantly tuning the electron trapper behavior as to circumvent the recombination of electron and hole. Consequently, the photo-activity of Cu_x–Ga_{1-x}/TiO_2 nanocomposites was optimized as long as they promote the rapid transfer of high-energy electrons in the catalytic structure.

4. Conclusions

Various laboratory-made photocatalysts have been comprehensively investigated by embedding titania substrates with copper and gallium dopants for the heterogeneous catalysis of CO_2 photoreduction. First, the XRD diffractograms exhibited that both Ga/Cu were doped into the TiO_2 substrate by conferring a crystalline microstructure. Second, TEM demonstrated that Cu_x–Ga_{1-x}/TiO_2 nanocomposites have particle sizes in the range 25–35 nm, and the elemental composition assessed by XPS unveiled the intrinsic binding energies of pure Ti, Cu and Ga ($2p_{3/2}$, $2p_{1/2}$). Afterwards, XANES patterns of gallium- and copper-doped nanocomposites revealed similar energy gaps and ascertained the doping phenomena, and indicated also narrower profiles obtained for the most active photocatalyst. 394.0 μmol-HCOOH/g_{cat} was produced after performing several photo-reduction experiments under different UV irradiation wavelengths and the highest selectivity was obtained with the $Cu_{0.78}$–$Ga_{0.22}/TiO_2$ nanocomposite. Hence, the photo-activity is improved due to a better distribution of Fermi levels and the formation of formic acid was maximized due to the prominent photocatalytic behavior exerted by the gallium and copper sites. These optimized the binding process with carbon dioxide and further coupled it with protons and photo-generated electrons encompassing a Cu^I and Cu^{II} redox couple.

Acknowledgment

The authors gratefully acknowledged the financial support of Fundação para a Ciência e Tecnologia, Portugal.

References

[1] B. Metz, O. Davidson, H. de Coninck, M. Loos, L. Meyer, IPCC Special Report on Carbon Dioxide Capture and Storage, Prepared by Working Group III of the Intergovernmental Panel on Climate Change, Cambridge University Press, New York, 2005, pp. 51–74.
[2] Z. Goren, I. Willner, A.J. Nelson, A.J. Frank, Journal of Physical Chemistry 94 (1990) 3784–3790.
[3] K. Hirano, K. Inoue, T. Yatsu, Journal of Photochemistry and Photobiology A 64 (1992) 255–258.
[4] O. Ishitani, C. Inoue, Y. Suzuki, T. Ibusuki, Journal of Photochemistry and Photobiology A 72 (1993) 269–271.
[5] T. Inoue, A. Fujishima, S. Konishi, K. Honda, Nature 277 (1979) 637–638.
[6] H. Inoue, H. Moriwaki, K. Maeda, H. Yoneyama, Journal of Photochemistry and Photobiology A 86 (1995) 191–196.
[7] I.H. Tseng, W.H. Chang, C.S. Jeffrey Wu, Applied Catalysis B 37 (2002) 37–48.
[8] C.H. Hung, B.J. Marinas, Environmental Science and Technology 31 (1997) 562–568.
[9] C.H. Hung, B.J. Marinas, Environmental Science and Technology 31 (1997) 1440–1445.
[10] K.H. Wang, H.H. Tsai, Y.H. Hsieh, Applied Catalysis B 17 (1998) 313–320.
[11] A. Strini, S. Cassese, L. Schiavi, Applied Catalysis B 61 (2005) 90–97.
[12] M. Anpo, H. Yamashita, Y. Ichihashi, S. Ehara, Journal of Electroanalytical Chemistry 396 (1995) 21–26.
[13] M. Anpo, H. Yamashita, K. Ikeue, Y. Fujii, S.G. Zhang, Y. Ichihashi, D.R. Park, Y. Suzuki, K. Koyano, T. Tatsumi, Catalysis Today 44 (1998) 327–332.
[14] Y. Kohno, H. Hayashi, S. Takenaka, T. Tanaka, T. Funabiki, S. Yoshida, Journal of Photochemistry and Photobiology A 126 (1999) 117–123.
[15] Y. Kohno, T. Tanaka, T. Funabiki, S. Yoshida, Physical Chemistry Chemical Physics 2 (2000) 2635–2639.
[16] H. Yoneyama, Catalysis Today 39 (1997) 169–175.
[17] S. Kaneco, H. Kurimoto, K. Ohta, T. Mizuno, A. Saji, Journal of Photochemistry and Photobiology A 109 (1997) 59–63.
[18] M. Subrahmanyam, S. Kaneco, N. Alonso-Vante, Applied Catalysis B 23 (1999) 169–174.
[19] K. Sayama, H. Arakawa, Journal of Physical Chemistry 97 (1993) 531–533.
[20] S. Yamagata, M. Nishijo, N. Murao, S. Ohta, I. Mizoguchi, Zeolites 15 (1995) 490–493.
[21] M.R. Nimlos, E.J. Wolfrum, M.L. Brewer, J.A. Fennell, G.B. Bintner, Environmental Science & Technology 30 (1996) 3102–3110.
[22] Y. Shioya, K. Ikeue, M. Ogawa, M. Anpo, Applied Catalysis A-General 254 (2003) 251–259.
[23] J.-S. Hwang, J.-S. Chang, S.-E. Park, K. Ikeue, M. Anpo, Studies in Surface Science and Catalysis 153 (2004) 299–302.
[24] H. Yamashita, M. Okazaki, K. Ikeue, M. Anpo, Studies in Surface Science and Catalysis 153 (2004) 289–294.
[25] K. Ikeue, S. Nozaki, M. Ogawa, M. Anpo, Catalysis Today 74 (2002) 241–248.
[26] I.H. Tseng, J.C.S. Wu, H.Y. Chou, Journal of Catalysis 221 (2004) 432–440.
[27] G. Li, S. Ciston, Z.V. Saponjic, L. Chen, N.M. Dimitrijevic, T. Rajh, K.A. Gray, Journal of Catalysis 253 (2008) 105–110.
[28] P.L. Richardson, M.L.N. Perdigoto, W. Wang, R.J.G. Lopes, Applied Catalysis B 126 (2012) 200–207.
[29] R.J.G. Lopes, M.L.N. Perdigoto, R.M. Quinta-Ferreira, Applied Catalysis B 117–118 (2012) 292–301.
[30] D. Wilson, W. Wang, R.J.G. Lopes, Applied Catalysis B 123–124 (2012) 273–281.
[31] H.-F. Chang, M.A. Saleque, W.-S. Hsu, W.-H. Lin, Journal of Molecular Catalysis 94 (1994) 233–242.
[32] G. Zschornack, Handbook of X-ray Data, Springer, Berlin/Heidelberg, 2007.